Global Character of Latent Heat Release in Oceanic Warm Rain Systems

Ethan L. Nelson[1] **and Tristan S. L'Ecuyer**[1]

[1] Department of Atmospheric and Oceanic Sciences, 1225 West Dayton Street, Madison, WI 53706.

Key Points:

- Warm rain is found to make up nearly 14% of tropical oceanic rainfall.
- Though less frequent, convective warm rain contributes as much column latent heating as stratiform.
- The height of maximum latent heat release is invariant across a wide range of environments.

Corresponding author: Ethan L. Nelson, `ethan.nelson@aos.wisc.edu`

Abstract

Warm rain plays an important role in Earth's water and energy cycles. Little is known, however, about the global character of latent heat release from warm rain regimes owing to a lack of satellite observations with sufficient sensitivity to this often light, sometimes isolated, precipitation. The Wisconsin Algorithm for Latent heating and Rainfall Using Satellites (WALRUS) utilizes CloudSat's W-band Cloud Profiling Radar to estimate vertical profiles of latent heating, surface rainfall rate, and related processes across all oceanic warm rain regimes. This study examines a four year climatology of monthly mean WALRUS estimates to document the global character of latent heating in oceanic warm rain and quantify the sensitivity of underlying condensation and evaporation processes to bulk properties of the large-scale environment.

Warm rain is found to make up 9.2% of oceanic global rainfall and 13.9% of oceanic tropical rainfall. Convective warm rain contributes 36% of rain accumulation and 50% of column latent heating even though its occurrence frequency is only 11%. Net pressure-weighted column-integrated latent heating from warm rain condensation averages 0.15 K day^{-1} of atmospheric heating, with nearly equal contribution from convective and shallow warm rain. While warm rain is found throughout the globe, the Intertropical Convergence Zone is a notable warm rain hot spot peaking near 1 K day^{-1}. The mean height of the maximum condensation in warm rain is 1.5 +/- 0.6 km, and found to be generally invariant to atmospheric stability. On the other hand, the depth of the entrainment cooling layer decreases with increasing inversion strength.

1 Introduction

Warm rain systems, precipitating clouds that reside below the freezing level that contain only liquid phase hydrometeors, are an important component of the trimodal tropical convection structure [e.g. *Battan and Braham*, 1956; *Johnson et al.*, 1999; *Liu and Zipser*, 2009; *Rapp et al.*, 2013]. But how much do they influence the hydrological and energy budgets of the planet? And what effect does the local environment have on the processes of hydrometeor formation, growth, and evaporation within warm rain? Answering these questions is necessary to understand the importance of and variation in, among other things, the positive shallow cloud feedback resulting from changes in cloud morphology in a warmer climate [*Hanson*, 1991; *Stephens*, 2005; *Randall et al.*, 2007; *Bony et al.*, 2015].

Warm rain contributes to tropical and global precipitation in the form of stratiform clouds and shallow convection. Passive satellite observations combined with data from the International Satellite Cloud Climatology Project (ISCCP) revealed 10%-20% of rainfall over the oceans between the 50^{o} latitudes was the result of warm rain [*Lin and Rossow*, 1997], and active observations from the Tropical Rainfall Measurement Mission (TRMM) in the subtropics contained around 20% of rainfall in the shallow category [*Short and Nakamura*, 2000]. Longer term analysis over nine years of combined TRMM active and passive data yielded an approximate 20% contribution by warm rain to tropical area precipitation [*Liu and Zipser*, 2009]. Most satellite sensors, however, are not able to completely sense the warm rain regime due not only to the light intensity of warm rain but also the shallow and often isolated nature of these clouds [*Behrangi et al.*, 2012; *Christensen et al.*, 2013; *Rapp et al.*, 2013]. *Berg et al.* [2010] estimate approximately 10% of rainfall–contributed by light rainfall–is missed by TRMM active instrument measurements when compared to CloudSat active instrument estimates.

These limitations have also prevented quantitative assessments of the latent heat release from warm rain processes. Latent heating plays a critical role in the Earth's climate by transferring energy between the surface and the atmosphere through phase changes of water. One important role of warm rain systems in the Earth's energy and water cycles is through the latent heat that is released from microphysical processes during hydrometeor formation and growth. While prior estimates from a collection of observations and datasets show latent heating accounts for approximately 98 W m^{-2} of the total energy budget over the oceans [*L'Ecuyer et al.*, 2015], regional differences in the vertical structure of this heating have not been completely diagnosed owing to the challenges in quantifying the warm rain component [*Zhang et al.*, 2010; *Jiang et al.*, 2011; *Ling and Zhang*, 2011]. Yet it is this movement of energy that drives the global water cycle by the processes of evaporation and sublimation to condensation and freezing and ultimately precipitation falling back to the surface.

In order to improve climate model parameterizations of the warm rain regimes that have partially escaped detection by some observations in the past [e.g. *Berg et al.*, 2010], alternative benchmarks need to be established that allow these model representations to be assessed. Misrepresenting clouds in the lower troposphere in GCMs can have implications on the energy budget, heat transport, and climate sensitivity because of their strong radiative impacts and the indications of possible morphological transitions in a warming climate [*Bony and Dufresne*, 2005; *Wyant et al.*, 2006; *Randall et al.*, 2007; *Xu et al.*, 2010; *Medeiros and Stevens*, 2011; *Gettelman et al.*, 2012; *Webb et al.*, 2013; *Vial et al.*, 2013; *Bretherton et al.*, 2013; *Brient and Bony*, 2013; *Zhang et al.*, 2013; *Nuijens et al.*, 2015; *Brient et al.*, 2016].

Rainfall is a key factor controlling cloud cover and radiative cloud properties, as clouds disappear while they rain out unless refreshed by some other source. Additionally, large-scale environmental characteristics, like vertical ascent or relative humidity, have a direct bearing on the role these clouds play in defining climate sensitivity [*Sherwood et al.*, 2014]. While constraints on cloud radiative effects are available from other sources [e.g. *Wielicki et al.*, 1996; *Zhang et al.*, 2004], no large-scale estimates of the condensational heating and evaporative cooling that are sensitive to warm clouds and rainfall in the atmosphere currently exist against which models may be evaluated.

We attempt to provide these estimates of warm rain falling globally over the oceans by leveraging CloudSat to infer cloud and precipitation processes through a model-based algorithm that quantifies their contribution to global rainfall over four years of observations. In filling this observational gap, we can document the prevalence of warm rain systems and stipulate how the environmental characteristics affect warm rain formation processes.

2 Data and Methods

2.1 Observations

With a sensitivity of nearly -30 dBZ and a vertical resolution of 240 m resulting from oversampling, the Cloud Profiling Radar (CPR), a W-Band nadir-pointing radar aboard CloudSat in the Afternoon Constellation (or A-Train), provides global vertical profiles of hydrometeors in the atmosphere [*Marchand et al.*, 2008; *Stephens et al.*, 2008; *Tanelli et al.*, 2008]. Previous work has demonstrated that CloudSat's high sensitivity and fine spatial resolution provide the ability to detect shallow and lightly precipitating clouds–characteristics of oceanic warm rain–except in cases where clouds do not reach the radar sensitivity threshold or lie within the lowest kilometer of the atmosphere and are masked by surface contamination of the radar return [*Kubar and Hartmann*, 2008; *Ellis et al.*, 2009; *Haynes et al.*, 2009; *Rapp et al.*, 2013].

Latent heat release can be quantified by many methods, including bulk estimates based on water and heating budgets over large regions and application of inverse methods that couple model simulations to more limited observations [*Reed and Recker*, 1971; *Yanai et al.*, 1973; *Johnson and Ciesielski*, 2000; *Schumacher et al.*, 2007]. The budget approach relies on closure constraints applied to radiosondes or other intensive observations, e.g. field campaigns, and is therefore limited both in time and in space. Conversely, the inverse method needs only a snapshot of the cloud and precipitation processes occurring at a given moment in time and employs a retrieval grounded in physical representations of the atmosphere. Thus, while less direct, the latter is more feasible for application to global-scale observations like those from a low Earth orbit satellite [e.g. *Yang and Smith*, 1999; *Shige et al.*, 2004; *Tao et al.*, 2016].

Following this general approach, *Nelson et al.* [2016] introduced the Wisconsin Algorithm for Latent Heating and Rainfall Using Satellites (or WALRUS) to quantify warm rain intensity and latent heating structure using CloudSat observations. WALRUS is a Bayesian retrieval coupled to cloud resolving model simulations using the Regional Atmospheric Atmospheric Modeling System (RAMS; *Cotton et al.* 2003; *Saleeby and van den Heever* 2013). The algorithm retrieves surface precipitation rate and vertical profiles of latent heating with a similar resolution to CloudSat of 1.5 km diameter footprint and 300 m vertical levels. The algorithm utilizes an *a priori* database that includes twelve oceanic warm rain RAMS simulations spanning a range of distinct maximum cloud condensation nuclei and forced sea surface temperature (SST) combinations (100 per cubic centimeter (cc^{-1}), 400 cc^{-1}, 800 cc^{-1}; 293 K, 298 K, and 303 K) allowing a wide range of atmospheric states to be represented in the algorithm [*Saleeby et al.*, 2015]. These simulations were performed at 250 m horizontal resolution and 100 m vertical resolution to resolve the warm rain systems, then downscaled to the retrieval resolution in line with CloudSat.

This study adopts the same observation vector defined in *Nelson et al.* [2016] that consists of both cloud vertical extent information (echo top height, rain top height, and maximum reflectivity height) and intensity information (path integrated reflectivity, near-surface reflectivity, and two way path integrated attenuation). Observed variables are mapped onto simulated radar observations corresponding to each RAMS profile in the database to produce an *a posteriori* distribution of the retrieved values, including vertically-resolved profiles of microphysical process rates and vertical velocity, liquid water path, surface rainfall rate, and other model variables associated with database profiles that best match the observed reflectivity structure. The retrieval solution is the weighted mean of the resulting distribution with uncertainty estimated to be the distribution spread. We refer the reader to *Nelson et al.* [2016] for more information about the simulation sampling and *a priori* offline database assembly.

Assumed errors are consistent with observation uncertainties and algorithm resolution: reflectivities are 1 dBZ, attenuations are 2 dB, and heights are 300 m. Since the reflectivity structure provides strong constraints on both the vertical structure of hydrometeors and column-integrated water content, errors in model physics are not likely to exert a prohibitive influence on the retrieval. The algorithm simply requires that the RAMS database adequately span a range of atmospheric scenes that may be encountered in nature and lets the observations define the relative frequency. Nevertheless, it is important to note that the process rates analyzed below derive from a model database. At worst, WALRUS can be considered as providing a framework for mapping state-of-the-art RAMS microphysics globally.

The implementation of WALRUS used here is based on the R04 CloudSat reflectivity and attenuation products [*CloudSat Data Processing Center*, 2007]. Only CloudSat data from 2007 through 2010 are analyzed since this is the time period when CloudSat was operating during both day and night. The full reflectivity profile from 2B-GEOPROF is used, but a conservative -22.5 dBZ minimum value is adopted to avoid false flags in cloud top heights due to noise. The attenuation values used from 2C-PRECIP-COLUMN are the hydrometeor attenuation product, which supplies estimates of the two-way attenuation to the surface resulting from hydrometeors based on surface backscatter; over the ocean, this has some dependence on the surface wind magnitude [*Haynes et al.*, 2009]. Freezing level information is drawn from the 2C-PRECIP-COLUMN freezing level product that is interpolated from ECMWF global analyses to the CloudSat orbit.

The WALRUS retrieval is run for all oceanic profiles with cloud tops lower than the freezing level and identifiable rainfall (defined as at least one vertical bin in the reflectivity profile reaching at least 0 dBZ). Figure 1 shows many of the products available from WALRUS from a warm rain segment of a CloudSat granule observed on April 17, 2007. Areas of deeper convective cumulus clouds correspond to taller profiles of latent heating and cooling as expected. Higher rain rate values coincide with areas of stronger evaporative cooling below the condensational layer. In addition, areas of strong updrafts can be identified with more intense and taller reflectivity structures. Finally, size and mixing ratio information segregates the profiles where cloud droplets and rain drops respectively dominate vertically. This retrieval sample shows that the algorithm handles a wide spectrum from stratus through trade cumulus as indicated by the differing cloud extents across a large extent of latitudes.

To demonstrate that the observations indeed provide constraints on the latent heating structures presented in the analysis that follows, it is worth taking a look at the diversity of characteristics from observations and comparing it to the retrieval database. A comparison of the parameter distributions between the database and observation profiles is displayed in Figure 2. Clearly the relative frequencies of occurrences differ between the database and observations. Furthermore, the distribution shape of observations varies between the full globe (Fig. 2(a)) and smaller regions (Fig. 2(b,c)). The distribution of observations is therefore able to sample distinctly different frequencies of database profiles as opposed to forcing the model distribution of atmospheric states onto reality. Or, put otherwise, there is clearly information content in the measurements to transform the *a priori* distribution into the different *a priori* distribution.

2.2 Ancillary Data

CloudSat's official rainfall rate products are used to quantify the frequency of occurrence of warm rain compared to all precipitation given the maturity of these datasets and previous efforts to validate them [*Ellis et al.*, 2009; *Smalley et al.*, 2014]. 2C-PRECIP-COLUMN identifies rainfall and estimates its intensity based on column integrated attenuation [*Haynes et al.*, 2009] while 2C-RAIN-PROFILE utilizes an optimal estimation approach to infer rainfall profiles based on attenuation-corrected reflectivity [*L'Ecuyer and Stephens*, 2002; *Mitrescu et al.*, 2010; *Lebsock and L'Ecuyer*, 2011]. Only profiles in which all algorithms successfully retrieve a solution are included in bias comparisons between CloudSat and WALRUS.

Global Precipitation Climatology Project (GPCP) monthly rainfall estimates can place the accumulation of warm rain into a broader hydrological context [*Adler et al.*, 2003; *Huffman et al.*, 2009]. GPCP is derived from merged polar-orbiting and geosynchronous satellite observations containing passive microwave and infrared instruments. Microwave polar-orbiting observations–sparsely distributed but of high resolution–are used to calibrate geosynchronous infrared observations that have much larger spatial coverage. Using GPCP provides global rainfall estimates independent of CloudSat that, in principle, include all forms of precipitation, providing a reference against which the fraction of global precipitation accumulation represented in the WALRUS product can be calculated.

There is considerable evidence that characteristics of the large-scale atmospheric dynamics affect the character of warm cloud and rain regimes [*Klein and Hartmann*, 1993; *Larson et al.*, 1999; *Wood and Bretherton*, 2006; *Sun et al.*, 2011; *Chung and Teixeira*, 2012; *Bretherton et al.*, 2013]. The sensitivity of warm rain processes inferred by WALRUS to dynamic and thermodynamic drivers is assessed using NASA's Modern Era Retrospective-Analysis for Research and Applications (MERRA; *Rienecker et al.* 2011). MERRA assimilates a wide array of environmental state data (e.g. winds, temperature, radiances) to provide a long-term reconstruction of the full atmosphere. MERRA vertical motion, inversion strength, and upper-level humidity are interpolated to each CloudSat field of view using a nearest neighbors approach [*Smalley and L'Ecuyer*, 2015].

To investigate the effect of the environment on the latent heating vertical structure, a number of parameters are chosen that are directly related to or derived from atmospheric state variables. Relative humidity at 700 mb (RH_{700}) provides information about the free tropospheric humidity. Vertical motion at 700 mb (ω_{700}) prescribes information about the character of circulation patterns in an area. Lower tropospheric stability (LTS) is a measure of the planetary boundary layer inversion strength defined as the difference of potential temperatures from the free troposphere and the surface, or $LTS = \theta_{700} - \theta_0$ [*Klein and Hartmann*, 1993]. Estimated inversion strength (EIS), defined as $EIS = LTS - \Gamma_m^{850}(z_{700} - LCL)$, uses LTS and the structure of the tropospheric thermodynamic profile to provide a more detailed measure of the inversion strength [*Wood and Bretherton*, 2006, Eq. 4].

2.3 Methods

WALRUS outputs are averaged to 2.5° x 2.5° and monthly resolution for the period from January 2007 to December 2010 to facilitate combination and comparisons with other datasets. Oceanic averages are computed by masking any grid boxes that contain land, and only grid boxes that contain at least 48 observations (approximately one per month) are selected for analysis to minimize poorly sampled grid boxes that may add noise.

In most cases, retrieved values are reported as the monthly mean across all available CloudSat observations. However, some aspects of the analysis utilize conditional means rather than the monthly mean. The conditional mean is the average value only for instances where a retrieval is performed, or $x_c = \sum_i^{N_w} x_i/N_w$, where N_w is the number of WALRUS retrievals. This quantity is useful for examining the behavior of the retrieval specifically, as opposed to the complete monthly contribution of a quantity over the course of the observation time period.

3 The global distribution of warm rain

The monthly mean global distribution of warm rainfall derived from WALRUS is shown in Figure 3(a). The warm rain components of large-scale features like the Intertropical Convergence Zone (ITCZ) are clearly present. Though the ITCZ is often visualized as a band of tall convection owing to its signature in infrared observations, WALRUS is able to demonstrate that it is comprised of convection of different shapes and sizes at various stages in their lifecycles. Some of the warm rain–particularly in convective areas–captured by WALRUS may eventually evolve to include an ice phase component, but at the observation time it had not yet glaciated and precipitation was still being generated through warm rain processes.

Mean warm rainfall amounts peak near 0.1 mm hr^{-1} just north of the Equator in the Pacific Ocean. Eastern ocean basin regions that coincide with the descending branch of the Hadley Cell and coastal upwelling also support higher warm rain accumulations with values ranging from 0.01 to 0.05 mm hr^{-1}. Overall, warm rain contributes 0.011 mm hr^{-1} (0.26 mm day^{-1}) of accumulation over the global oceans.

The frequency of WALRUS retrievals from all profiles that CloudSat observes is documented in Figure 3(b). The highest sampling, nearly 8% of all observations, occurs off the western coast of South America. With the exception of the Equatorial region in the East Pacific Ocean Basin, observations are favored in areas of the descending branch of the Hadley Cell in both the Northern and Southern Hemispheres, except in the immediate vicinity of the coast where clouds may go undetected by CloudSat either due to the blind zone or because they are extremely light [*Rapp et al.*, 2013]. Fractions tail off moving poleward as more precipitation falls from mixed phase precipitation processes that reached the freezing level.

The average intensity of warm rain, or conditional mean warm rain rates, are presented in Figure 3(c). Warm rain intensities are more uniform than the mean accumulations in Figure 3(a), averaging 0.5 mm hr^{-1} in many locations with areas of enhanced instantaneous rain rates exceeding 1 mm hr^{-1} north of the Equator in the Pacific Ocean basin. In regions along the west coasts of the continents and along the Equator, conditional rain rates are locally depressed where the stratocumulus decks are most prevalent.

Comparing the rainfall rate distribution retrieved from WALRUS against GPCP (Fig. 3(d)), warm rain explains 9.2% of the total GPCP rainfall accumulation over the oceans. Subsidence regions in the eastern ocean basin regions are almost entirely comprised of warm rain. Restricting to the area between the 50^{o} latitudes, the average WALRUS percentage of warm rainfall over the oceans is 11.0%. Further restricting the averaging area to the tropics bounded by 25^{o} latitudes yields a percentage of warm rainfall over the oceans of 13.9%. The percentage grows when focusing on the tropical regions because warm rain fractions are near zero in the midlatitudes and polar regions indicating that cold precipitation processes dominate in these areas. If areas in which WALRUS exceeds GPCP are reduced to the GPCP rainfall values, oceanic warm rainfall fractions of total precipitation become 8.8%, 10.4%, and 12.9% for the globe, within 50^{o} latitudes, and within 25^{o} latitudes, respectively.

It should be noted that the requirements for defining warm rain in WALRUS are more conservative than those applied in the CloudSat 2C-PRECIP-COLUMN algorithm [*Haynes et al.*, 2009]. The latter often considers profiles labeled *rain possibly* containing drizzle, but Figure 3(e) indicates that WALRUS does not currently include some of these drizzling profiles. Future latent heating estimates may need to consider lightly drizzling and non-precipitating scenes to fully capture the effects of condensation and evaporation on the vertical structure of atmospheric heating in warm rain.

To illustrate that the RAMS database does not introduce large global biases in WALRUS warm rain retrievals, the estimates in Figure 3(c) are compared with those obtained from 2C-RAIN-PROFILE in Figure 3(f). WALRUS retrieves slightly higher rainfall rates in the north- and southeastern ocean basins than the 2C-RAIN-PROFILE product while rates in the Equatorial ocean basins are lower. Globally, WALRUS warm rain estimates are 12.1% lower than the 2C-RAIN-PROFILE algorithm over the oceans.

Though warm rain is present over much of the globe's oceans, liquid clouds exhibit widely varying characteristics as evidenced in part by the variation in rain rate. Both stratocumulus decks and shallow convection produce warm rain but they form in different large-scale environments that dictate their evolution. It can be expected that these two cloud types will have different latent heating profile characteristics since their vertical extents and intensities are different. To better distinguish these distinct warm rain regimes, we introduce a simple classification based on WALRUS retrievals of in-cloud vertical velocity: profiles with a retrieved maximum vertical velocity greater than or equal to 1 m s^{-1} are considered "shallow convective" or, simply, convective warm rain and profiles with a maximum vertical velocity less than 1 m s^{-1} are stratiform warm rain.

This follows the generalized definition defined by *Yuter and Houze* [1995] who defined convective conditions to occur when vertical velocity exceeds ~1-3 m s^{-1}, as well as large eddy simluation (LES) work by *Khairoutdinov et al.* [2009] and *Zhu* [2015] who define convective updrafts as places that exceed 1 m s^{-1}. The partitioning of retrieved profiles between these categories is shown in Figures 3(g) and (h), but because the cut-off is somewhat subjective, these regime separations are not exact. Convection is most frequently observed in the ITCZ as well as along the eastern coast of the Asian continent.

Globally, convective constitutes only about 11% of all warm rain occurrences but it comprises 36% of warm rain accumulation.

4 Global latent heat release in warm rain processes

4.1 Spatial distributions

Given its consistency with existing rainfall products, WALRUS provides an ideal resource for quantifying the global distribution of latent heating owing to warm rain processes. Mean vertically resolved profiles of latent heating and cooling are column pressure weighted based on a standard atmosphere to yield the monthly mean column-integrated latent heating by warm rain shown in Figure 4(a). Over the world's oceans, the average latent heating and cooling combined is 0.15 K day^{-1}. It is apparent that warm rain contributes to atmospheric heating nearly globally. Like the distribution of global mean warm rain, the largest contributions of latent heating from warm rain are found in the ITCZ, reaching nearly 1 K day^{-1} in the East Pacific, with lower maxima occurring in the subsidence regions of all major ocean basins. Regions immediately off the coasts in the East Pacific and Atlantic Oceans that are characterized by stratus decks exhibit local minima in total heating and cooling. Small amounts of warm rain latent heating from postfrontal warm systems are also retrieved in areas extending into the midlatitudes, but the fraction of rain at these latitudes originating from warm rain processes is low (Fig. 3(d)). When converting latent heating to an equivalent rainfall flux and comparing with the retrieved rainfall rate on a monthly mean scale (not shown), latent heating is slightly underestimated for mean rain rates above 0.04 mm hr^{-1} while values tend to straddle the predicted relationship below that.

Next, the components of the average latent heating profiles owing to condensation and evaporation processes are separated in Figures 4(b) and (c). Notwithstanding differences in environmental conditions, the presence of more heating in a column (Fig. 4(b)) generally means there is more column liquid water than can be evaporated (Fig. 4(c)). Evaporation may exceed the rate of condensation due to entrainment at the cloud top or sides, which is the process by which clouds are eroded through mixing with dry environmental air [*Wood*, 2012]. Additionally, as rain falls from the base of the cloud toward the surface, it encounters drier environmental air that evaporates raindrops. An extreme example of the latter case is virga, a phenomenon that occurs when precipitation is completely evaporated prior to reaching the surface.

This ability to separately diagnose heating and cooling regions using WALRUS provides additional insights into the relative importance of specific processes in warm rain scenes. Figure 4(d) shows the ratio of cooling below the cloud from rain evaporation to heating from the condensation layer by further separating the cooling from Figure 4(c). It should be noted that the separation into below and above condensational layer heating is only generated when heating exists within one contiguous layer. *Wyant et al.* [1997] found that modeled stratocumulus evolved into trade cumulus when SST was increased due to a moistening of the boundary layer. This is generally in line with other studies of the stratocumulus to cumulus evolution [e.g *Sandu and Stevens*, 2011; *Tsai and Wu*, 2016]. A similar pattern is evident here as the ratio of evaporation to heating decreases as one moves westward away from the eastern coastal regions, where clouds transition from stratocumulus to shallow trade cumulus. This suggests that the decreased ratio is caused primarily by enhanced rain evaporation to heating near the continents, while the higher ratios further into the ocean basin are the result of less rainfall evaporation.

4.2 Vertical structure of heating

Differences in the magnitude of cooling processes below and above the heating layer in Figure 4(d) hint at variations in the vertical structure of latent heating and cooling in warm rain across the globe. In Figure 5, the structure of the mean latent heating profile is shown for boxes in the East Central Pacific (5^{o}S-5^{o}N, 100^{o}W-95^{o}W) and the Southeastern Pacific (20^{o}S-15^{o}S, 100^{o}W-95^{o}W). Profiles are separated into convective and stratiform regimes as described before according to profile maximum vertical velocity and both the four year conditional averages and total monthly means are shown. Focusing first on the East Central Pacific, convective latent heating profiles are more intense and vertically developed than stratiform profiles (Fig. 5(a), left side). But, because convective profiles occur about 10% of the time in this region over the four years, stratiform profiles tend to dominate the occurrence-weighted mean (Fig. 5(a), right side).

Figure 5(b) shows that there is significant regional variability in the relative importance of convective and stratiform warm rain even in the same longitude stripe but displaced to the south in a subsidence region. The fraction of retrieved profiles classified as convective decreases from 10% to 4%, which is reflected in a decreasing relative contribution to the mean latent heating profile in spite of the conditionally larger heating retrieved in convective profiles. Yet another factor in the difference in the average profile for all regimes between these two regions is the fact that the absolute occurrence of warm rain is nearly triple that observed in the East Central box owing to the increased prevalence of warm rain in that area. Nevertheless, stratiform regime profiles are still more prevalent and therefore exert a stronger influence on the mean warm rain latent heating structure for both regions.

A comparison of each regime's relative contribution to the vertical structure of latent heating is examined on the global scale. Figure 6 shows the global mean latent heating and cooling distributions in 900-m thick layers, starting near the ground and extending upwards. A strength of the Bayesian approach used in WALRUS is that it is less affected by ground clutter that obscures satellite observations below 1 km; parameters observed above the clutter region are used to extrapolate information down to the ground using the database. This is especially highlighted in the lowest layer, where boundary layer cooling due to rain evaporation dominates the globe. The layer between 0.9 and 1.8 km above the ground approximately corresponds to the layer of strongest condensational heating. The 1.8-2.7 km layer begins to differentiate warm rain regimes: cooling is prevalent in the stratus decks in coastal regions in eastern ocean basins as well as in the midlatitudes, while trade cumulus in the ITCZ and SPCZ still exhibit latent heating associated with hydrometeor formation and growth at this height. The dipole structure at this level may be an indication of the shallow meridional circulation in the Tropical Eastern Pacific as described by *Zhang et al.* [2004]. All regions are characterized by cloud top evaporation in 2.7-3.6 km with cooling replacing any of the areas of heating from the layer below. Weak cloud top cooling remains in only some of the taller warm rain regions between 3.6-4.5 km, and by 4.5-5.4 km cloud top cooling is only realized in Equatorial warm rain.

The vertical structures of heating from convective and stratiform warm rain are compared more directly in Figures 7 and Figure 8. Convective profiles exhibit less evaporative cooling below the cloud base in 0-1 km compared to the analogous stratiform profiles. The convective profiles also contribute more condensational heating from 1.8-2.7 km and lack the presence of a heating–cooling dipole across ocean basins. Cooling at upper levels is also lower in magnitude in the convective cases due to the lower frequency of occurrence. Averaged layers from stratiform profiles continue to show the dipole character possibly from the shallow meridional circulation of the Tropical Eastern Pacific, indicating inter-regime variability exists in different dynamical regimes. Nevertheless, these characteristics describe general differences in the character of the processes retrieved between these two different regimes that have been defined by the retrieved vertical velocity. This fact is further reflected in the difference in latent heating contribution between the regimes, as the mean column integrated latent heating contribution from convective rain is 0.078 K day^{-1} while that from stratiform rain is 0.076 K day^{-1}.

4.3 Seasonal cycle

It has previously been documented that stratus clouds in the subtropics exhibit a seasonal cycle, generally peaking in coverage in the season of highest thermodynamic stability [*Klein and Hartmann*, 1993]. To examine whether a similar variation exists in warm rain latent heating over the course of the seasonal cycle, the zonally averaged oceanic distribution of warm rain column latent heating is decomposed into seasons in Figure 9. The zonal distribution of the yearly mean and most seasons shows the greatest heating north of the Equator with a local minimum just south of the Equator. The distribution of heating is asymmetric between the hemispheres with larger values occurring in the subsidence regions in the winter hemisphere. For transition seasons of spring and fall in the subtropics, the Southern Hemisphere contributes a larger magnitude of latent heating. Nevertheless, the overall pattern favors the subtropics and just north of the Equator as areas of largest heating throughout the year implying that the general circulation is a strong influence on where the warm rain occurs.

Each hemisphere respectively exhibits a pattern in the seasonal cycle. While the subtropics peak in the winter, the higher latitudes peak around the summer months. This is likely the case because the warm summer clouds over the ocean contributed by baroclinic cyclones are replaced by cold winter precipitation at these latitudes. In both hemispheres, the seasons that are favored to reach a maximum reverse at around the 30^{o} part, appearing to coincide with edge of the Hadley cell in the general circulation.

5 Environmental drivers

The preceding climatologies can be used to evaluate the current representation of warm rain processes in models. But, to offer a pathway toward improving model physics, the responses of warm rain processes to environmental drivers must be quantified. Previous studies have suggested that environmental stability metrics serve as good predictors for cloud cover and type in both models [*Chung and Teixeira*, 2012; *Bretherton et al.*, 2013] and observations [*Klein and Hartmann*, 1993; *Larson et al.*, 1999; *Wood and Bretherton*, 2006; *Sun et al.*, 2011]. It can then be expected that the processes by which these clouds are ultimately generated should similarly be constrained by the environmental stability.

5.1 Distributions of environment and (in)stability

Monthly averaged values of three MERRA environmental parameters conditionally sampled to retrieved WALRUS scenes are shown in Figure 10 . All three indicators exhibit similar behaviors to a first order given that they all provide a measure of climatic regime. Values of RH_{700} (Fig. 10(a)) are lower in the subsiding regions of the Hadley cell extending from the eastern ocean basins Equator- and westward. Higher humidities are present just north of the Equator across the globe, extending south from the Equator in the West Pacific Ocean, and in northwestern ocean basins. ω_{700} (Fig. 10(c)) shows a similar distribution of subsidence in the areas containing lower humidity and large-scale ascent collocated with areas of higher humidities. EIS (Fig. 10(e)), which is calculated as introduced in Section 2, follows the pattern of higher stability in subsiding regions and lower stability in convective regions.

The difference of each environmental parameter between times when warm rain is retrieved and all CloudSat observations is shown on the right side of Figure 10. Fig. 10(b), showing the RH_{700} difference, indicates that areas around the Equator have elevated moisture levels at 700 mb when warm rain is found compared to all CloudSat observations. These regions also extend to eastern coasts of North America and Asia. ω_{700} and EIS are preferred to be slightly less stable in similar regions at the Equator. On the other hand, some areas of large-scale subsidence exhibit slightly higher EIS and slightly lower

RH_{700} in cases of warm rain compared to the background state. Though the difference distributions are noisy, they support general meteorological conditions that give preference toward the different warm rain regimes shown in Figures 3(g) and (h), with areas of a larger fraction of shallow convective precipitation in areas of enhanced relative humidity and areas of a larger stratiform fraction in areas of enhanced stability.

5.2 Instability and cloud processes

To better understand the impact of these environmental drivers on the latent heating profiles, we next examine mean profiles of evaporative cooling and condensational heating over the range of each parameter. Figure 11 shows how the mean structure of latent heating and cooling vary as a function of MERRA RH_{700}, ω_{700}, and EIS. Increased relative humidity aloft yields taller cloud extents, while a drier upper atmosphere has a shallower top with stronger evaporative cooling (Fig. 11(a)). ω_{700}, describing vertical motion, compresses the vertical depth of the profile (Fig. 11(b)). As the vertical motion intensifies, indicating stronger subsidence, the layer becomes more compressed vertically. EIS encapsulates these behaviors of a decrease in the cloud height extent, a decrease in heating, and a decrease in cooling with increasing EIS as well (Fig. 11(c)). These relationships broadly follow theoretical models of cloud-topped boundary layers [e.g. *Lilly*, 1968; *Stevens*, 2002], that boundary layer depth is a function of entrainment and vertical motion. Yet in each of these cases, the height of maximum heating seems to be less variant than the cooling layer.

To describe changes in the overall character of the latent heating relationships with stability, joint histograms of maximum cooling height, cloud top cooling thickness, evaporation below to above ratio, maximum heating height, and heating thickness with EIS are synthesized in Figure 12 on a monthly timescale. The behavior of some of these parameters is as expected. Increased stability yields a decreased height of maximum cooling (Fig. 12(a)), a narrower cloud top cooling thickness (Fig. 12(b)), increased relative importance of evaporation below cloud base compared to entrainment above the heating layer (Fig. 12(c)), and some narrowing of the condensation layer thickness (Fig. 12(e)). These behaviors show an increase in stability prevents rain systems from expanding in height, generally following models of cloud-topped boundary layer evolution as before. However, the retrieved height of maximum latent heat release in condensation remains within the same general vicinity despite changes in stability (Fig. 12(d)). Globally, the height of maximum condensational heating in warm rain is estimated to be 1.5 +/- 0.6 km .

The separation of these parameters for the two different warm rain regimes reveals different but related behaviors (Fig. 12, right side). Convection with stronger updrafts ostensibly extend the convective plume to a higher vertical level compared to stratiform, increasing the thickness of the condensation layer. By spreading the condensation higher into the atmosphere, the height of maximum entrainment is displaced higher and the depth of entrainment decreases due to the intruding condensation. With a reduction in entrainment, its efficiency compared to evaporation below the cloud base is reduced and convective clouds have higher evaporation to entrainment ratios. Conversely, less stable regions for stratiform clouds will tend to indicate a moistened boundary layer compared to more stable, meaning the ratio of evaporation will be lower in lower EIS conditions.

Therefore, we see that the environment plays a strong role–in depth and in placement–of the evaporative cooling characteristics, as does the warm rain regime, while the level of maximum latent heating is nearly constant even among differing regimes (Fig. 12(d)). LESes compiled in *Blossey et al.* [2016] for the CFMIP/GASS Intercomparison of Large eddy and Single column models also show that, even in a 4xCO_2 perturbation simulation, the vertical distribution of the heating in precipitating shallow cumulus are somewhat invariant on a long time scale. This may be an important characteristic of warm rain that is captured by both climate models and observations that warrants further observation and exploration on smaller spatiotemporal scales in the future.

6 Conclusions

A four year (2007-2010) climatology of latent heating and cooling for oceanic warm rain systems has been established based on CloudSat CPR observations. Because of the CPR's sensitivity to clouds and light precipitation, we can observe and estimate the impact that may otherwise be underestimated or missed in other estimates as evidenced by *Berg et al.* [2010]. Warm rain makes up nearly 9.2% of precipitation accumulation over the oceans and comprises nearly 14% of tropical rainfall (bounded by 25^o latitudes). Convective warm rain, defined as profiles where the in-cloud vertical velocity exceeds 1 m s^{-1} in any height bin, constitutes 11% of warm rain occurrence but yields more than a third of the total warm rain accumulation. Net warm rain condensational processes contribute 0.15 K day^{-1} (7.44 W m^{-2}) of heating globally on average to the atmosphere, accounting for 7.6% of the total atmospheric latent heating contribution over the oceans estimated in *L'Ecuyer et al.* [2015] and nearly matching the difference between observed and optimal estimation constrained latent heating estimates.

The character of the vertical profile of latent heating and cooling varies substantially across the globe on a monthly timescale, with areas of environmental instability yielding deeper evaporative layers than those in more stable environments. Regions vary not only in the heights of cooling from entrainment but also in the ratio of cooling below and above the heating layer, which stems from the regime of warm rain occurring. There is much less variation in the layer of net heating, which generally resides consistently between 1 and 2 km suggesting that condensation processes are less sensitive to changes in stability than evaporation associated with cloud top entrainment. Column latent heating and cooling varies substantially on seasonal time scales, with hemispheric winters contributing more overall heating than the respective hemispheric summers. Contributions from convective and stratiform rain to the global mean latent heating are nearly equal in spite of their different frequencies of occurrence.

Most of the statistics here have been calculated on a global scale. While there is variability even at this scale, results suggest that examining regions at a smaller than global scale may reveal finer details masked in large-scale averages. This was broadly evidenced in intercomparisons between two regions of the same ocean basin in Figure 5 with differences appearing in regimes' relative contributions to latent heating based on the location zonally and also in the joint distributions of these quantities with environmental stability in Figure 12. A better understanding of the variability regionally and between different regions of the same climatic regime may improve modeling efforts of morphology transitions in a warming climate.

It is important to note that, because this analysis is based on observations from a sun-synchronous satellite, the results may be biased due to the sampling time of day and revisit time of the satellite. CloudSat crosses the Equator at 1:30 (AM/PM) local time so the diurnal cycle that exists in warm rain [e.g. *Rozendaal et al.*, 1995] is not completely sampled. Additionally, CloudSat is unable to sense clouds and precipitation that do not reach the sensitive detectability threshold of the CPR or lie below about 1 km due to ground backscatter of the radar signal. This means that warm rain wholly confined to the lowest kilometer of the troposphere is missed by CloudSat [*Rapp et al.*, 2013] and therefore this analysis.

Compared to previous latent heating estimates [e.g. *Tao et al.*, 2016], however, WALRUS provides significant evidence for the importance of considering warm rain in the context of global rainfall and cloud condensation processes. Looking toward warming climates, the environmental dependencies of latent heating and cooling touched on here are likely to have an effect on the warm rain morphologies and distributions that evolve globally. For example, the results suggest that future changes in atmospheric stability are likely to exert a greater impact on the depth of evaporative cooling than the height of maximum latent heating. Yet establishing the true climatology of warm rain is still difficult given the recent launch of CloudSat only a decade ago and its limited remaining lifetime. Future sensors with a high sensitivity to clouds and light rain are therefore important to continuing this important record and further documenting the effects warm rain has on the global climate and the feedbacks therein.

Acknowledgments

This work was supported by NASA CloudSat/CALIPSO Science Team Grant #NNX13AQ32G, NASA ACE Grant #NNX13AK08G, and NASA Headquarters under the NASA Earth and Space Science Fellowship Program Grant #NNX14AL35H. WALRUS data are available at https://lecuyer.aos.wisc.edu/WALRUS/.

References

Adler, R. F., G. J. Huffman, A. Chang, R. Ferraro, P.-P. Xie, J. Janowiak, B. Rudolf, U. Schneider, S. Curtis, D. Bolvin, A. Gruber, J. Susskind, P. Arkin, and E. Nelkin (2003), The version-2 Global Precipitation Climatology Project (GPCP) monthly precipitation analysis (1979–Present), *J. Hydrometeor.*, *4*(6), 1147–1167, doi:10.1175/1525-7541(2003)004<1147:TVGPCP>2.0.CO;2.

Battan, L. J., and R. R. Braham (1956), A study of convective precipitation based on cloud and radar observations, *J. Meteor.*, *13*(6), 587–591, doi:10.1175/1520-0469(1956)013<0587:ASOCPB>2.0.CO;2.

Behrangi, A., M. Lebsock, S. Wong, and B. Lambrigtsen (2012), On the quantification of oceanic rainfall using spaceborne sensors, *J. Geophys. Res.*, *117*(D20), D20,105, doi:10.1029/2012JD017979.

Berg, W., T. L'Ecuyer, and J. M. Haynes (2010), The distribution of rainfall over oceans from spaceborne radars, *J. Appl. Meteor. Climatol.*, *49*, 535–543, doi:10.1175/2009JAMC2330.1.

Blossey, P. N., C. S. Bretherton, A. Cheng, S. Endo, T. Heus, A. P. Lock, and J. J. van der Dussen (2016), CGILS Phase 2 LES intercomparison of response of subtropical marine low cloud regimes to CO2 quadrupling and a CMIP3 composite forcing change, *J. Adv. Model. Earth Sys.*, *8*(4), 1714–1726, doi:10.1002/2016MS000765.

Bony, S., and J.-L. Dufresne (2005), Marine boundary layer clouds at the heart of tropical cloud feedback uncertainties in climate models, *Geophys. Res. Lett.*, *32*(20), L20B06, doi:10.1029/2005GL023851.

Bony, S., B. Stevens, D. M. W. Frierson, C. Jakob, M. Kageyama, R. Pincus, T. G. Shepherd, S. C. Sherwood, A. P. Siebesma, A. H. Sobel, M. Watanabe, and M. J. Webb (2015), Clouds, circulation and climate sensitivity, *Nature Geosci.*, *8*(4), 261–268, doi:10.1038/ngeo2398.

Bretherton, C. S., P. N. Blossey, and C. R. Jones (2013), Mechanisms of marine low cloud sensitivity to idealized climate perturbations: A single-LES exploration extending the CGILS cases, *J. Adv. Model. Earth Sys.*, *5*(2), 316–337, doi:10.1002/jame.20019.

Brient, F., and S. Bony (2013), Interpretation of the positive low-cloud feedback predicted by a climate model under global warming, *Climate Dyn.*, *40*, 2415–2431, doi:10.1007/s00382-011-1279-7.

Brient, F., T. Schneider, Z. Tan, S. Bony, X. Qu, and A. Hall (2016), Shallowness of tropical low clouds as a predictor of climate models' response to warming, *Climate Dyn.*, *47*, 433–449, doi:10.1007/s00382-015-2846-0.

Christensen, M. W., G. L. Stephens, and M. D. Lebsock (2013), Exposing biases in retrieved low cloud properties from CloudSat: A guide for evaluating observations and climate data, *J. Geophys. Res.*, *118*(21), 12120–12131, doi:10.1002/2013JD020224.

Chung, D., and J. Teixeira (2012), A simple model for stratocumulus to shallow cumulus cloud transitions, *J. Climate*, *25*, 2547–2554, doi:10.1175/JCLI-D-11-00105.1.

CloudSat Data Processing Center (2007), Cloudsat level 2 and level 3 data, release 4, Available online at http://www.cloudsat.cira.colostate.edu/data-products.

Cotton, W. R., R. A. Pielke Sr., R. L. Walko, G. E. Liston, C. J. Tremback, H. Jiang, R. L. McAnelly, J. Y. Harrington, M. E. Nicholls, G. G. Carrio, and J. P. McFadden (2003), RAMS 2001: Current status and future directions, *Meteor. Atmos. Phys.*, *82*, 5–29, doi:10.1007/s00703-001-0584-9.

Ellis, T. D., T. S. L'Ecuyer, J. M. Haynes, and G. L. Stephens (2009), How often does it rain over the global oceans? The perspective from CloudSat, *Geophys. Res. Lett.*, *36*(3), L03,815, doi:10.1029/2008GL036728.

Gettelman, A., J. E. Kay, and K. M. Shell (2012), The evolution of climate sensitivity and climate feedbacks in the Community Atmosphere Model, *J. Climate*, *25*, 1453–1469, doi:10.1175/JCLI-D-11-00197.1.

Hanson, H. P. (1991), Marine stratocumulus climatologies, *International Journal of Climatology*, *11*(2), 147–164, doi:10.1002/joc.3370110204.

Haynes, J. M., T. S. L'Ecuyer, G. L. Stephens, S. D. Miller, C. Mitrescu, N. B. Wood, and S. Tanelli (2009), Rainfall retrieval over the ocean with spaceborne W-band radar, *J. Geophys. Res.*, *114*, D00A22, doi:10.1029/2008JD009973.

Huffman, G. J., R. F. Adler, D. T. Bolvin, and G. Gu (2009), Improving the global precipitation record: GPCP version 2.1, *Geophys. Res. Lett.*, *36*(17), L17808, doi: 10.1029/2009GL040000.

Jiang, X., D. E. Waliser, W. S. Olson, W.-K. Tao, T. S. L'Ecuyer, K.-F. Li, Y. L. Yung, S. Shige, S. Lang, and Y. N. Takayabu (2011), Vertical diabatic heating structure of the MJO: Intercomparison between recent reanalyses and TRMM estimates, *Mon. Wea. Rev.*, *139*, 3208–3223, doi:10.1175/2011MWR3636.1.

Johnson, R. H., and P. E. Ciesielski (2000), Rainfall and radiative heating rates from TOGA COARE atmospheric budgets, *J. Atmos. Sci.*, *57*, 1497–1514, doi:10.1175/1520-0469(2000)057<1497:RARHRF>2.0.CO;2.

Johnson, R. H., T. M. Rickenbach, S. A. Rutledge, P. E. Ciesielski, and W. H. Schubert (1999), Trimodal characteristics of tropical convection, *J. Climate*, *12*, 2397–2418, doi: 10.1175/1520-0442(1999)012<2397:TCOTC>2.0.CO;2.

Khairoutdinov, M. F., S. K. Krueger, C.-H. Moeng, P. A. Bogenschutz, and D. A. Randall (2009), Large-eddy simulation of maritime deep tropical convection, *J. Adv. Model. Earth Syst.*, *1*(15), doi:10.3894/JAMES.2009.1.15.

Klein, S. A., and D. L. Hartmann (1993), The seasonal cycle of low stratiform clouds, *J. Climate*, *6*(8), 1587–1606, doi:10.1175/1520-0442(1993)006<1587:TSCOLS>2.0.CO;2.

Kubar, T. L., and D. L. Hartmann (2008), Vertical structure of tropical oceanic convective clouds and its relation to precipitation, *Geophys. Res. Lett.*, *35*(3), L03,804, doi: 10.1029/2007GL032811.

Larson, K., D. L. Hartmann, and S. A. Klein (1999), The role of clouds, water vapor, circulation, and boundary layer structure in the sensitivity of the tropical climate, *J. Climate*, *12*, 2359–2374, doi:10.1175/1520-0442(1999)012<2359:TROCWV>2.0.CO;2.

Lebsock, M. D., and T. S. L'Ecuyer (2011), The retrieval of warm rain from CloudSat, *J. Geophys. Res.*, *116*(D20), D20,209, doi:10.1029/2011JD016076.

L'Ecuyer, T. S., and G. L. Stephens (2002), An estimation-based precipitation retrieval algorithm for attenuating radars, *J. Appl. Meteor.*, *41*(3), 272–285, doi:10.1175/1520-0450(2002)041<0272:AEBPRA>2.0.CO;2.

L'Ecuyer, T. S., H. K. Beaudoing, M. Rodell, W. Olson, B. Lin, S. Kato, C. A. Clayson, E. Wood, J. Sheffield, R. Adler, G. Huffman, M. Bosilovich, G. Gu, F. Robertson, P. R. Houser, D. Chambers, J. S. Famiglietti, E. Fetzer, W. T. Liu, X. Gao, C. A. Schlosser, E. Clark, D. P. Lettenmaier, and K. Hilburn (2015), The observed state of the energy budget in the early Twenty-First Century, *J. Climate*, *28*(21), 8319–8346, doi: 10.1175/JCLI-D-14-00556.1.

Lilly, D. K. (1968), Models of cloud-topped mixed layers under a strong inversion, *Quart. J. Roy. Meteor. Soc.*, *94*, 292–309, doi:10.1002/qj.49709440106.

Lin, B., and W. B. Rossow (1997), Precipitation water path and rainfall rate estimates over oceans using special sensor microwave imager and International Satellite Cloud Climatology Project data, *J. Geophys. Res.*, *102*(D8), 9359–9374, doi:10.1029/96JD03987.

Ling, J., and C. Zhang (2011), Structural evolution in heating profiles of the MJO in global reanalyses and TRMM retrievals, *J. Climate*, *24*(3), 825–842, doi: 10.1175/2010JCLI3826.1.

Liu, C., and E. J. Zipser (2009), "Warm rain" in the Tropics: Seasonal and regional distributions based on 9 yr of TRMM data, *J. Climate*, *22*, 767–779, doi: 10.1175/2008JCLI2641.1.

Marchand, R., G. G. Mace, T. Ackerman, and G. Stephens (2008), Hydrometeor detection using CloudSat–an Earth-orbiting 94-GHz cloud radar, *J. Atmos. Oceanic Technol.*, *25*, 519–533, doi:10.1175/2007JTECHA1006.1.

Medeiros, B., and B. Stevens (2011), Revealing differences in GCM representations of low clouds, *Climate Dyn.*, *36*, 385–399, doi:10.1007/s00382-009-0694-5.

Mitrescu, C., T. L'Ecuyer, J. Haynes, S. Miller, and J. Turk (2010), Cloudsat precipitation profiling algorithm–model description, *J. Appl. Meteor. Climatol.*, *49*, 991–1003, doi: 10.1175/2009JAMC2181.1.

Nelson, E. L., T. S. L'Ecuyer, S. M. Saleeby, W. Berg, S. R. Herbener, and S. C. van den Heever (2016), Toward an algorithm for estimating latent heat release in warm rain systems, *J. Atmos. Oceanic Technol.*, *33*, 1309–1329, doi:10.1175/JTECH-D-15-0205.1.

Nuijens, L., B. Medeiros, I. Sandu, and M. Ahlgrimm (2015), The behavior of trade-wind cloudiness in observations and models: The major cloud components and their variability, *J. Adv. Model. Earth Sys.*, *7*, 600–616, doi:10.1002/2014MS000390.

Randall, D., R. Wood, S. Bony, R. Colman, T. Fichefet, J. Fyfe, V. Kattsov, A. Pitman, J. Shukla, J. Srinivasan, R. Stouffer, A. Sumi, and K. Taylor (2007), Climate models and their evaluation, in *Climate Change 2007: The physical science basis. Contribution of Working Group I to the Fourth Assessment Report of the Intergovernmental Panel on Climate Change*, edited by S. Solomon, D. Qin, M. Manning, Z. Chen, M. Marquis, K. Averyt, M.Tignor, and H. Miller, pp. 589–662, Cambridge University Press, Cambridge.

Rapp, A. D., M. Lebsock, and T. L'Ecuyer (2013), Low cloud precipitation climatology in the southeastern Pacific marine stratocumulus region using CloudSat, *Env. Res. Lett.*, *8*, 014027, doi:10.1088/1748-9326/8/1/014027.

Reed, R. J., and E. E. Recker (1971), Structure and properties of synoptic-scale wave disturbances in the Equatorial Western Pacific, *J. Atmos. Sci.*, *28*, 1117–1133, doi: 10.1175/1520-0469(1971)028<1117:SAPOSS>2.0.CO;2.

Rienecker, M. M., M. J. Suarez, R. Gelaro, R. Todling, J. Bacmeister, E. Liu, M. G. Bosilovich, S. D. Schubert, L. Takacs, G.-K. Kim, S. Bloom, J. Chen, D. Collins, A. Conaty, A. da Silva, W. Gu, J. Joiner, R. D. Koster, R. Lucchesi, A. Molod, T. Owens, S. Pawson, P. Pegion, C. R. Redder, R. Reichle, F. R. Robertson, A. G. Ruddick, M. Sienkiewicz, and J. Woollen (2011), MERRA: NASA's Modern-Era Retrospective Analysis for Research and Applications, *J. Climate*, *24*, 3624–3648, doi: 10.1175/JCLI-D-11-00015.1.

Rozendaal, M. A., C. B. Leovy, and S. A. Klein (1995), An observational study of diurnal variations of marine stratiform cloud, *J. Climate*, *8*, 1795–1809, doi:10.1175/1520-0442(1995)008<1795:AOSODV>2.0.CO;2.

Saleeby, S. M., and S. C. van den Heever (2013), Developments in the CSU-RAMS aerosol model: Emissions, nucleation, regeneration, deposition, and radiation, *J. Appl. Meteor. Climatol.*, *52*, 2601–2622, doi:10.1175/JAMC-D-12-0312.1.

Saleeby, S. M., S. R. Herbener, S. C. van den Heever, and T. S. L'Ecuyer (2015), Impacts of cloud droplet nucleating aerosols on shallow tropical convection, *J. Atmos. Sci.*, *72*, 1369–1385, doi:10.1175/JAS-D-14-0153.1.

Sandu, I., and B. Stevens (2011), On the factors modulating the stratocumulus to cumulus transitions, *J. Atmos. Sci.*, *68*, 1865–1881, doi:10.1175/2011JAS3614.1.

Schumacher, C., M. H. Zhang, and P. E. Ciesielski (2007), Heating structures of the TRMM field campaigns, *J. Atmos. Sci.*, *64*, 2593–2610, doi:10.1175/JAS3938.1.

Sherwood, S. C., S. Bony, and J.-L. Dufresne (2014), Spread in model climate sensitivity traced to atmospheric convective mixing, *Nature*, *505*, 37–42, doi: doi:10.1038/nature12829.

Shige, S., Y. N. Takayabu, W.-K. Tao, and D. E. Johnson (2004), Spectral retrieval of latent heating profiles from TRMM PR data. Part I: Development of a model-based algorithm, *J. Appl. Meteor.*, *43*(8), 1095–1113, doi:10.1175/1520-0450(2004)043<1095:SROLHP>2.0.CO;2.

Short, D. A. and K. Nakamura (2000), TRMM radar observations of shallow precipitation over the tropical oceans, *J. Climate*, *13*, 4107–4124, doi:10.1175/1520-0442(2000)013<4107:TROOSP>2.0.CO;2.

Smalley, M., and T. L'Ecuyer (2015), A global assessment of the spatial distribution of precipitation occurrence, *J. Appl. Meteor. Climatol.*, *54*, 2179–2197, doi:10.1175/JAMC-D-15-0019.1.

Smalley, M., T. L'Ecuyer, M. Lebsock, and J. Haynes (2014), A comparison of precipitation occurrence from the NCEP Stage IV QPE Product and the CloudSat Cloud Profiling Radar, *J. Hydrometeor.*, *15*, 444–458, doi:10.1175/JHM-D-13-048.1.

Stephens, G. L. (2005), Cloud feedbacks in the climate system: A critical review, *J. Climate*, *18*(2), 237–273, doi:10.1175/JCLI-3243.1.

Stephens, G. L., D. G. Vane, S. Tanelli, E. Im, S. Durden, M. Rokey, D. Reinke, P. Partain, G. G. Mace, R. Austin, T. L'Ecuyer, J. Haynes, M. Lebsock, K. Suzuki, D. Waliser, D. Wu, J. Kay, A. Gettelman, Z. Wang, and R. Marchand (2008), CloudSat mission: Performance and early science after the first year of operation, *J. Geophys. Res.*, *113*, D00A18, doi:10.1029/2008JD009982.

Stevens, B. (2002), Entrainment in stratocumulus-topped mixed layers, *Quart. J. Roy. Meteor. Soc.*, *128*, 2663–2690, doi:10.1256/qj.01.202.

Sun, F., A. Hall, and X. Qu (2011), On the relationship between low cloud variability and lower tropospheric stability in the Southeast Pacific, *Atmos. Chem. Phys.*, *11*, 9053–9065, doi:10.5194/acp-11-9053-2011.

Tanelli, S., S. L. Durden, E. Im, K. S. Pak, D. G. Reinke, P. Partain, J. M. Haynes, and R. T. Marchand (2008), CloudSat's Cloud Profiling Radar after two years in orbit: Performance, calibration, and processing, *IEEE Trans. Geosci. Remote Sensing*, *46*, 3560–3573, doi:10.1109/TGRS.2008.2002030.

Tao, W.-K., Y. N. Takayabu, S. Lang, S. Shige, W. Olson, A. Hou, G. Skofronick-Jackson, X. Jiang, C. Zhang, W. Lau, T. Krishnamurti, D. Waliser, M. Grecu, P. E. Ciesielski, R. H. Johnson, R. Houze, R. Kakar, K. Nakamura, S. Braun, S. Hagos, R. Oki, and A. Bhardwaj (2016), TRMM latent heating retrieval: Applications and comparisons with field campaigns and large-scale analyses, *Meteor. Monogr.*, *56*, 2.1–2.34, doi: 10.1175/AMSMONOGRAPHS-D-15-0013.1.

Tsai, J.-Y., and C.-M. Wu (2016), Critical transitions of stratocumulus dynamical systems due to perturbation in free-atmosphere moisture, *Dyn. Atm. Oceans*, *76*, 1–13, doi: 10.1016/j.dynatmoce.2016.08.002.

Vial, J., J.-L. Dufresne, and S. Bony (2013), On the interpretation of inter-model spread in CMIP5 climate sensitivity estimates, *Climate Dyn.*, *41*, 3339–3362, doi:10.1007/s00382-013-1725-9.

Webb, M. J., F. H. Lambert, and J. M. Gregory (2013), Origins of differences in climate sensitivity, forcing and feedback in climate models, *Climate Dyn.*, *40*, 677–707, doi: 10.1007/s00382-012-1336-x.

Wielicki, B. A., B. R. Barkstrom, E. F. Harrison, R. B. Lee III, G. L. Smith, and J. E. Cooper (1996), Clouds and the Earth's Radiant Energy System (CERES): An Earth observing system experiment, *Bull. Amer. Meteor. Soc.*, *77*, 853–868, doi:10.1175/1520-

0477(1996)077<0853:CATERE>2.0.CO;2.

Wood, R. (2012), Stratocumulus clouds, *Mon. Wea. Rev.*, *140*, 2373–2423, doi: 10.1175/MWR-D-11-00121.1.

Wood, R., and C. S. Bretherton (2006), On the relationship between stratiform low cloud cover and lower-tropospheric stability, *J. Climate*, *19*, 6425–6432, doi: 10.1175/JCLI3988.1.

Wyant, M., C. Bretherton, H. Rand, and D. Stevens (1997), Numerical simulations and a conceptual model of the stratocumulus to trade cumulus transition, *J. Atmos. Sci.*, *54*, 168–192, doi:10.1175/1520-0469(1997)054<0168:NSAACM>2.0.CO;2.

Wyant, M. C., C. S. Bretherton, J. T. Bacmeister, J. T. Kiehl, I. M. Held, M. Zhao, S. A. Klein, and B. J. Soden (2006), A comparison of low-latitude cloud properties and their response to climate change in three AGCMs sorted into regimes using mid-tropospheric vertical velocity, *Climate Dyn.*, *27*(2), 261–279, doi:10.1007/s00382-006-0138-4.

Xu, K.-M., A. Cheng, and M. Zhang (2010), Cloud-resolving simulation of low-cloud feedback to an increase in sea surface temperature, *J. Atmos. Sci.*, *67*, 730–748, doi: 10.1175/2009JAS3239.1.

Yanai, M., S. Esbensen, and J.-H. Chu (1973), Determination of bulk properties of tropical cloud clusters from large-scale heat and moisture budgets, *J. Atmos. Sci.*, *30*, 611–627, doi:10.1175/1520-0469(1973)030<0611:DOBPOT>2.0.CO;2.

Yang, S., and E. A. Smith (1999), Four-dimensional structure of monthly latent heating derived from SSM/ISatellite measurements, *J. Climate*, *12*(4), 1016–1037, doi: 10.1175/1520-0442(1999)012<1016:FDSOML>2.0.CO;2.

Yuter, S. E., and R. A. Houze. Jr. (1995), Three-dimensional kinematic and microphysical evolution of Florida cumulonimbus. Part I: Spatial distribution of updrafts, downdrafts, and precipitation, *Mon. Wea. Rev.*, *123*(7), 1921–1940, doi:10.1175/1520-0493(1995)123<1921:TDKAME>2.0.CO;2.

Zhang, C., J. Ling, S. Hagos, W.-K. Tao, S. Lang, Y. N. Takayabu, S. Shige, M. Katsumata, W. S. Olson, and T. L'Ecuyer (2010), MJO signals in latent heating: Results from TRMM retrievals, *J. Atmos. Sci.*, *67*(11), 3488–3508, doi:10.1175/2010JAS3398.1.

Zhang, C., M. McGauley, and N. A. Bond (2004), Shallow meridional circulation in the Tropical Eastern Pacific, *J. Climate*, *17*, 133–139, doi:10.1175/1520-0442(2004)017<0133:SMCITT>2.0.CO;2.

Zhang, M., C. S. Bretherton, P. N. Blossey, P. H. Austin, J. T. Bacmeister, S. Bony, F. Brient, S. K. Cheedela, A. Cheng, A. D. Del Genio, S. R. De Roode, S. Endo, C. N. Franklin, J.-C. Golaz, C. Hannay, T. Heus, F. A. Isotta, J.-L. Dufresne, I.-S. Kang, H. Kawai, M. Köhler, V. E. Larson, Y. Liu, A. P. Lock, U. Lohmann, M. F. Khairoutdinov, A. M. Molod, R. A. J. Neggers, P. Rasch, I. Sandu, R. Senkbeil, A. P. Siebesma, C. Siegenthaler-Le Drian, B. Stevens, M. J. Suarez, K.-M. Xu, K. von Salzen, M. J. Webb, A. Wolf, and M. Zhao (2013), CGILS: Results from the first phase of an international project to understand the physical mechanisms of low cloud feedbacks in single column models, *J. Adv. Model. Earth Sys.*, *5*(4), 826–842, doi:10.1002/2013MS000246.

Zhang, Y., W. B. Rossow, A. A. Lacis, V. Oinas, and M. I. Mishchenko (2004), Calculation of radiative fluxes from the surface to top of atmosphere based on ISCCP and other global data sets: Refinements of the radiative transfer model and the input data, *J. Geophys. Res.*, *109*(D19), D19105, doi:10.1029/2003JD004457.

Zhu, P. (2015), On the mass-flux representation of vertical transport in moist convection, *J. Atmos. Sci.*, *72*, 4445–4468, doi:10.1175/JAS-D-14-0332.1.

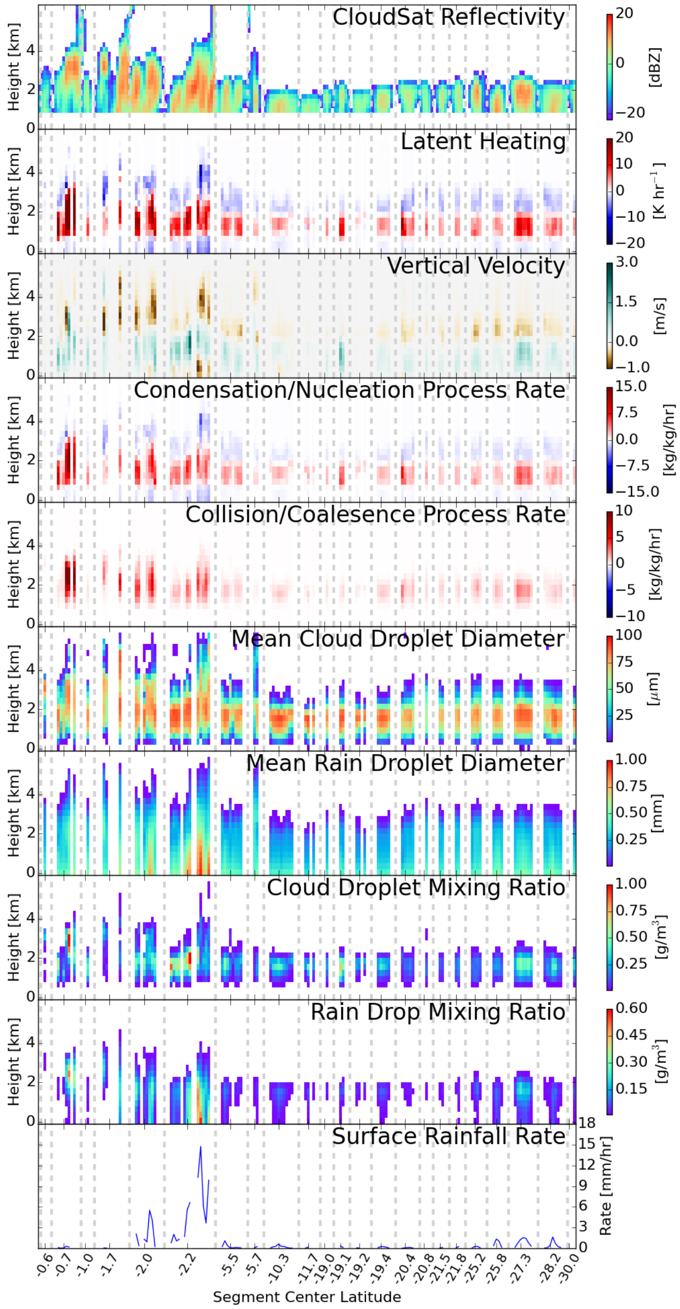

Figure 1. Example WALRUS retrieval on part of CloudSat granule #05151 showing the algorithm outputs available. Segments where more than five profiles are not retrieved are truncated (indicated by gray dashed lines) for easier viewing. The top panel shows the CloudSat reflectivity used as input for the algorithm and subsequent plots display latent heating (positive values condensational heating, negative values evaporative cooling), vertical velocity (positive values up, negative values down), condensation process rate (positive values condensation, negative values evaporation), collision and coalesence process rate, cloud mean diameter, rain drop mean diameter, cloud droplet mixing ratio, rain drop mixing ratio, and surface rainfall rate.

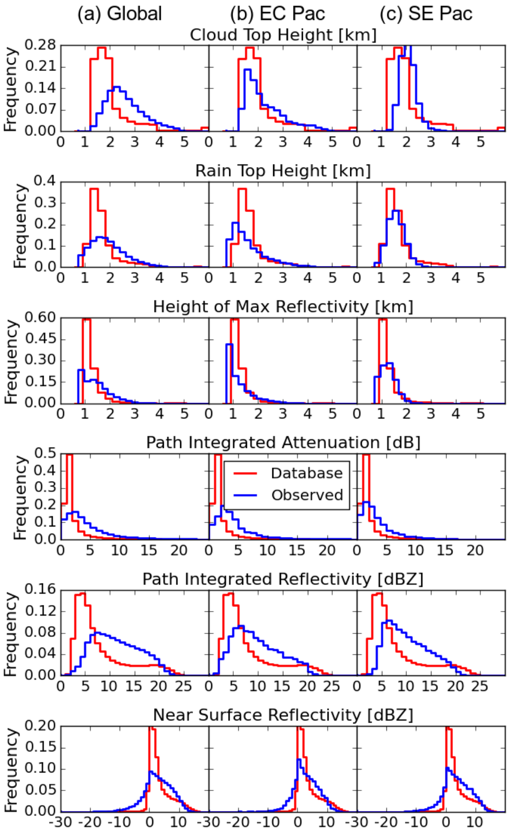

Figure 2. Distributions of WALRUS observation vector parameters in the WALRUS database (blue) and from CloudSat profiles used in this study for 2007-2010 (red): (a) globally, (b) in the East Central Pacific Ocean Basin (5^{o}S–0^o, 100^{o}W–95^{o}W), and (c) in the Southeast Pacific Ocean Basin (20^{o}S–15^{o}S, 100^{o}W–95^{o}W).

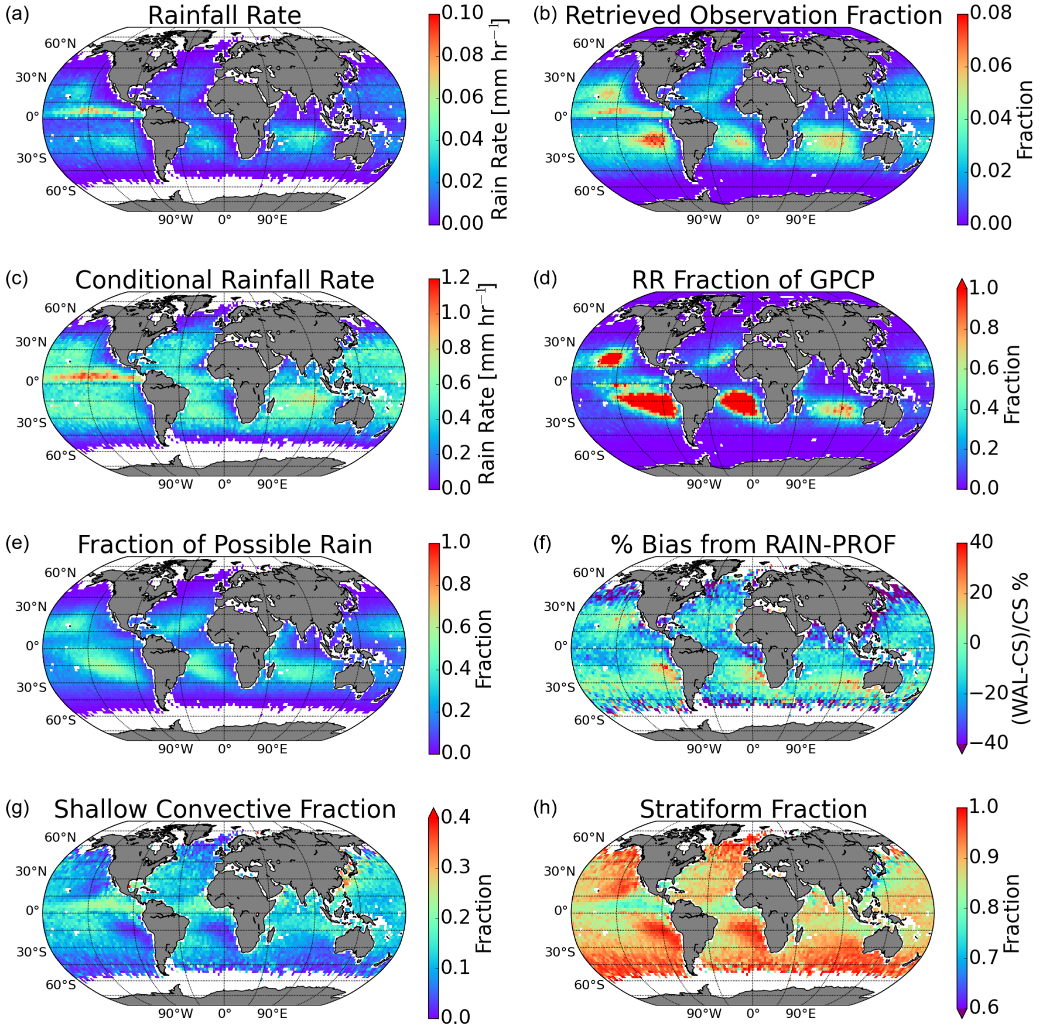

Figure 3. (a) Monthly average warm rainfall. (b) Fraction of all observed CloudSat profiles retrieved as warm rain for this time period. (c) Conditionally averaged warm rainfall rate. (d) Fraction of average GPCP monthly rainfall accumulation contributed by warm rain. (e) Fraction of possibly rain profiles according to 2C-PRECIP-COLUMN that are retrieved as warm rain by WALRUS for this time period. (f) Monthly average bias percentage of WALRUS conditional rainfall from 2C-RAIN-PROFILE CloudSat product. Fraction of retrieved profiles classified as (g) "shallow convective" and (h) stratiform in this study.

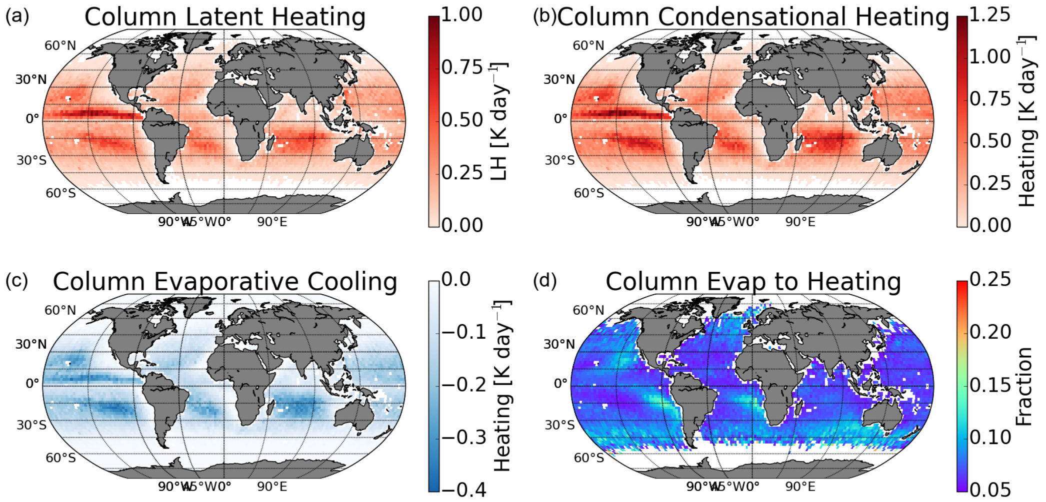

Figure 4. Global distributions of monthly averaged warm rain processes. (a) Column latent heating from condensation and evaporation. (b) Column latent heating from condensation only. (c) Column latent cooling from evaporation and entrainment only. (d) Ratio of cooling below the heating layer to the magnitude of the heating layer.

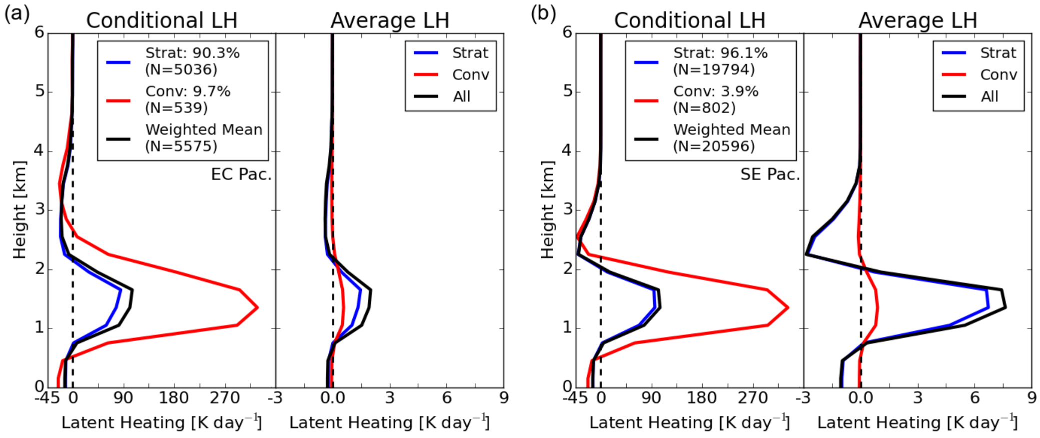

Figure 5. Profiles of latent heating taken as a four year conditional average of retrievals (left) and as the monthly mean over all observations (right) for (a) a box over the East Central Pacific (5^{o}S-5^{o}N, 100^{o}W-95^{o}W) and (b) a box over the Southeastern Pacific Ocean (20^{o}S–15^{o}S, 100^{o}W–95^{o}W). Conditional plots include a weighted mean based on the regime frequencies of occurrence shown in the legend, while average plots show the total contribution by both regimes.

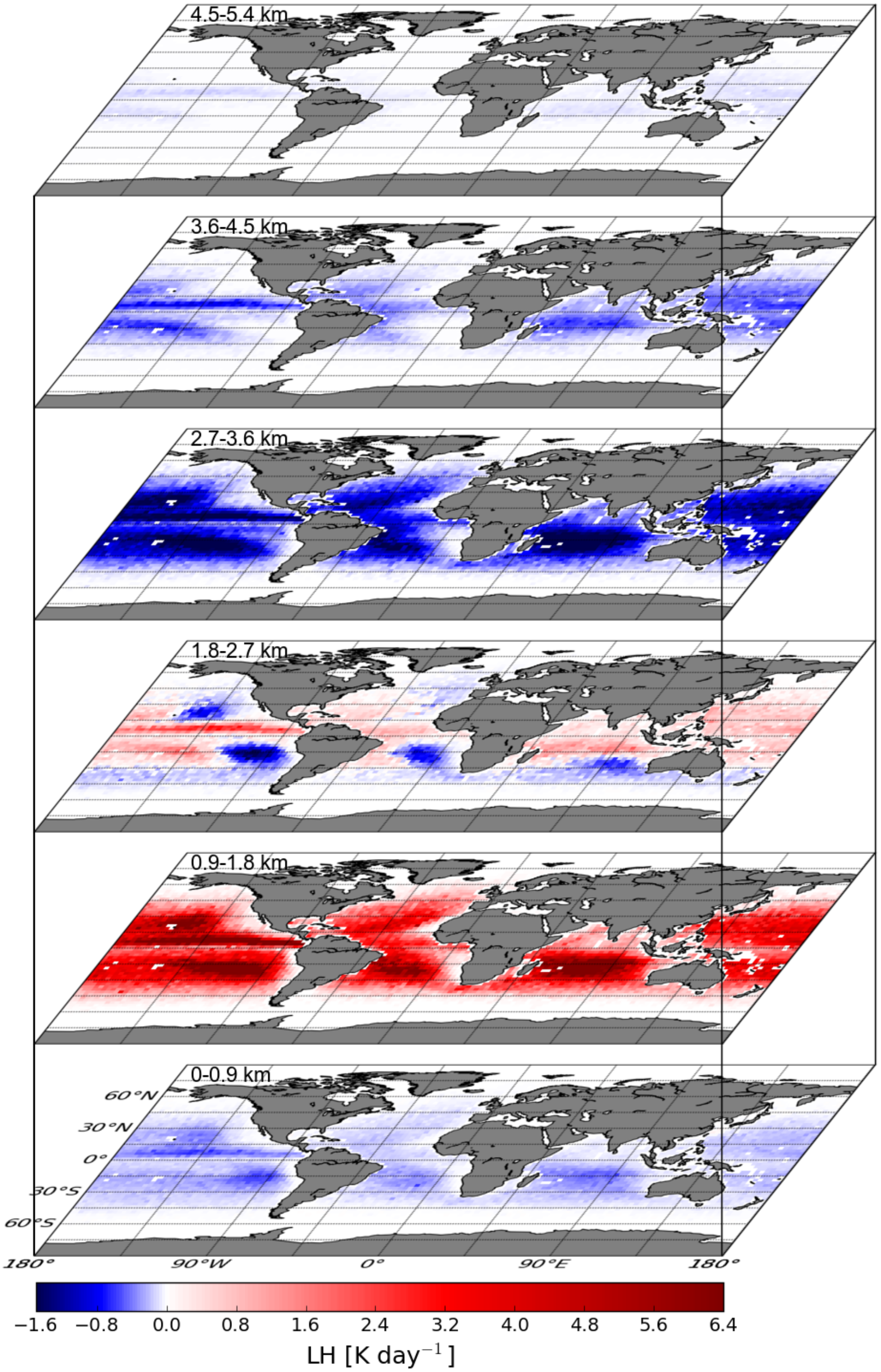

Figure 6. A vertical cross section of the mean monthly global latent heating distribution averaged in approximately one kilometer layers.

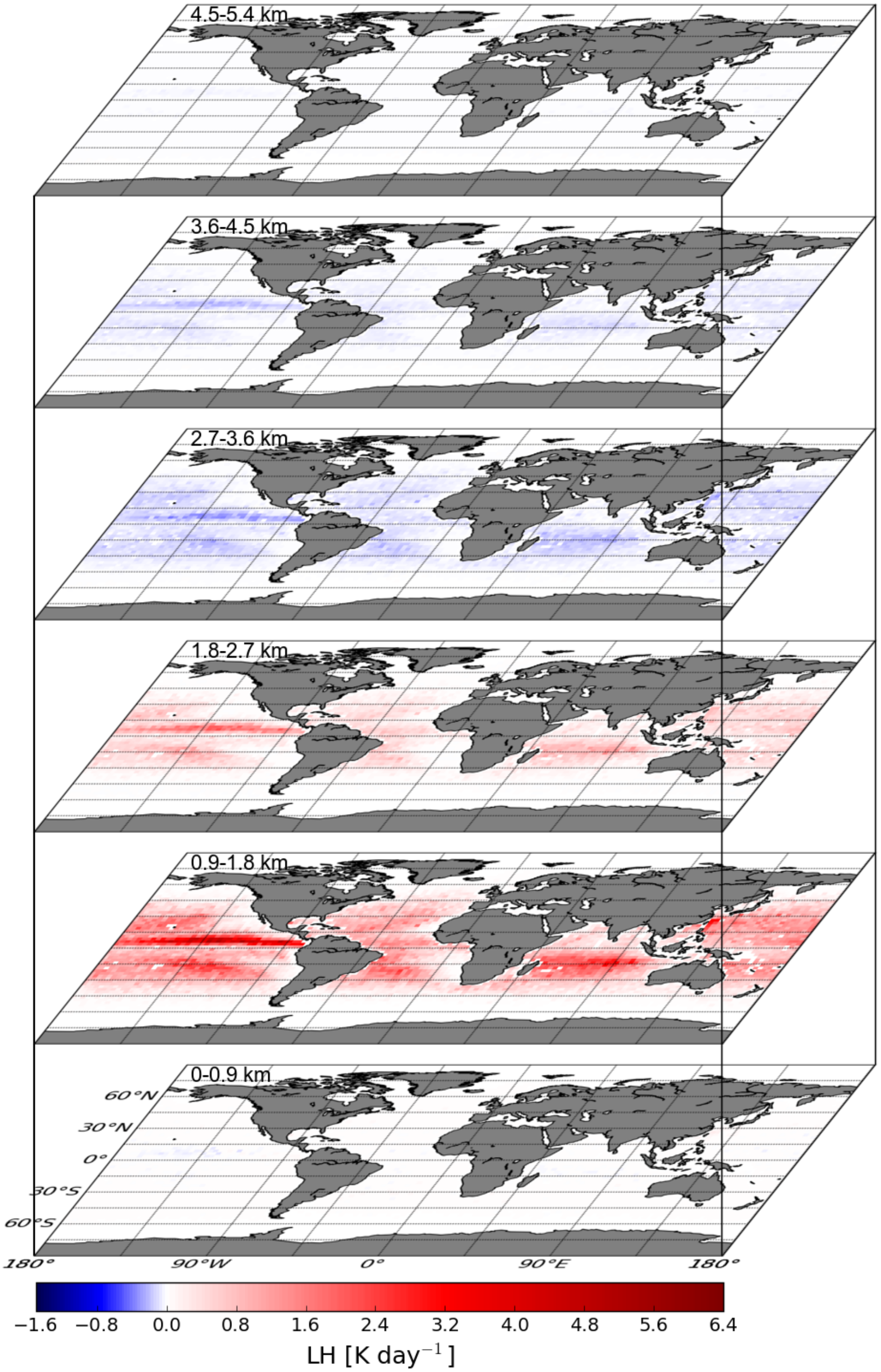

Figure 7. As in Figure 6 but only for profiles with a maximum vertical velocity greater than or equal to 1 m/s representing regimes more characteristic of convection.

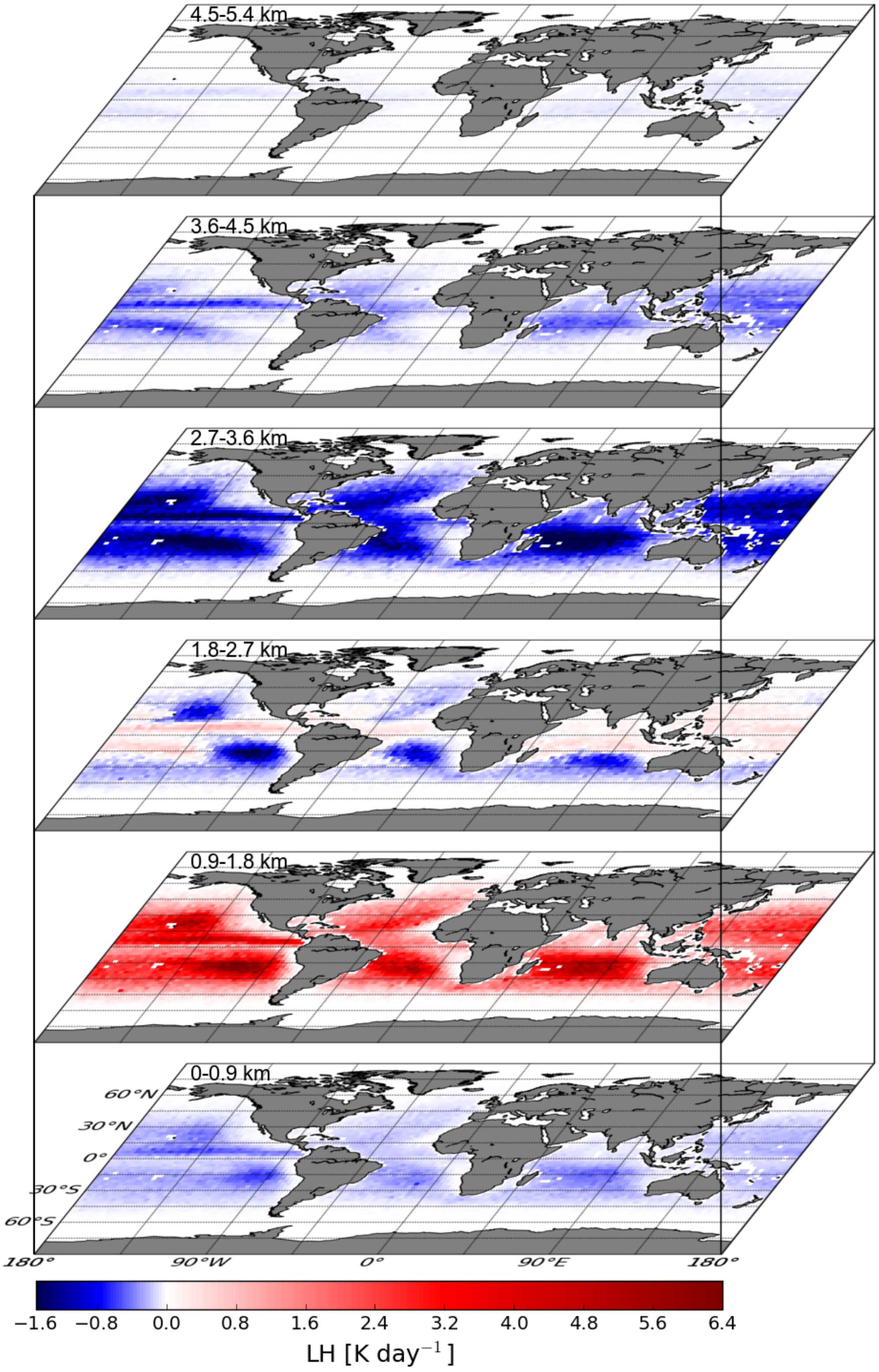

Figure 8. As in Figure 6 but only for profiles with a maximum vertical velocity less than 1 m/s representing more stratiform regimes.

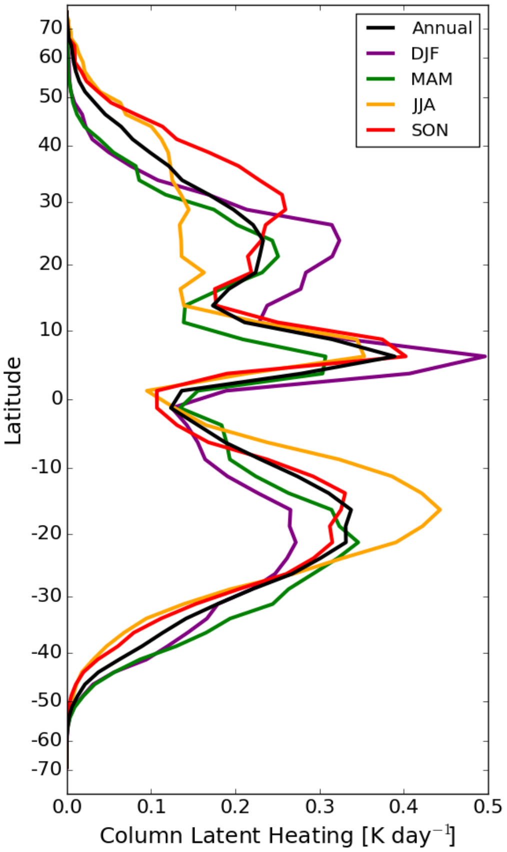

Figure 9. Zonal distribution of the monthly mean column latent heating for the full annual cycle (black) and months that comprise each season (see legend).

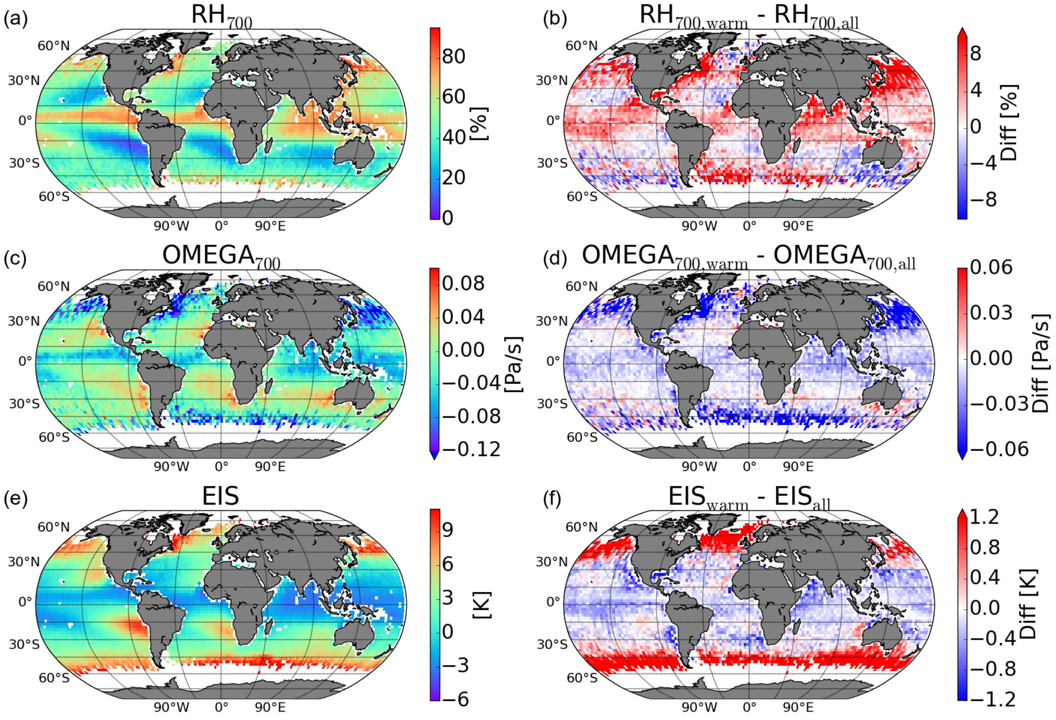

Figure 10. Monthly conditionally averaged MERRA parameters for instances where warm rain was retrieved: (a) relative humidity at 700 mb, (c) vertical velocity at 700 mb, and (e) EIS. The respective monthly mean differences for each variable between warm rain scenes and all scenes are displayed in (b), (d), and (f).

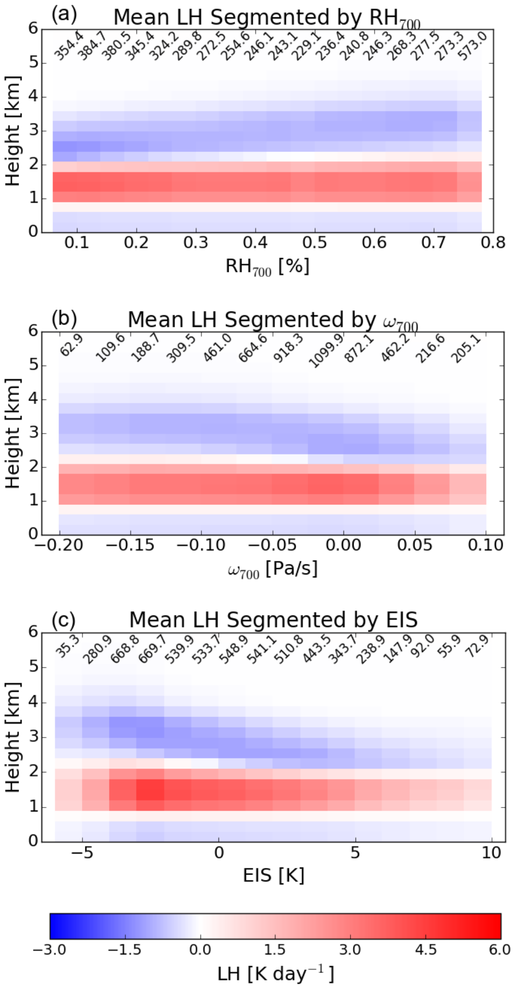

Figure 11. Distributions of monthly mean latent heating and cooling profiles binned by conditionally averaged MERRA parameters of (a) RH at 700 mb, (b) ω at 700 mb, and (c) EIS. The number of warm rain scenes in each bin is noted at the top of each bin profile (in thousands).

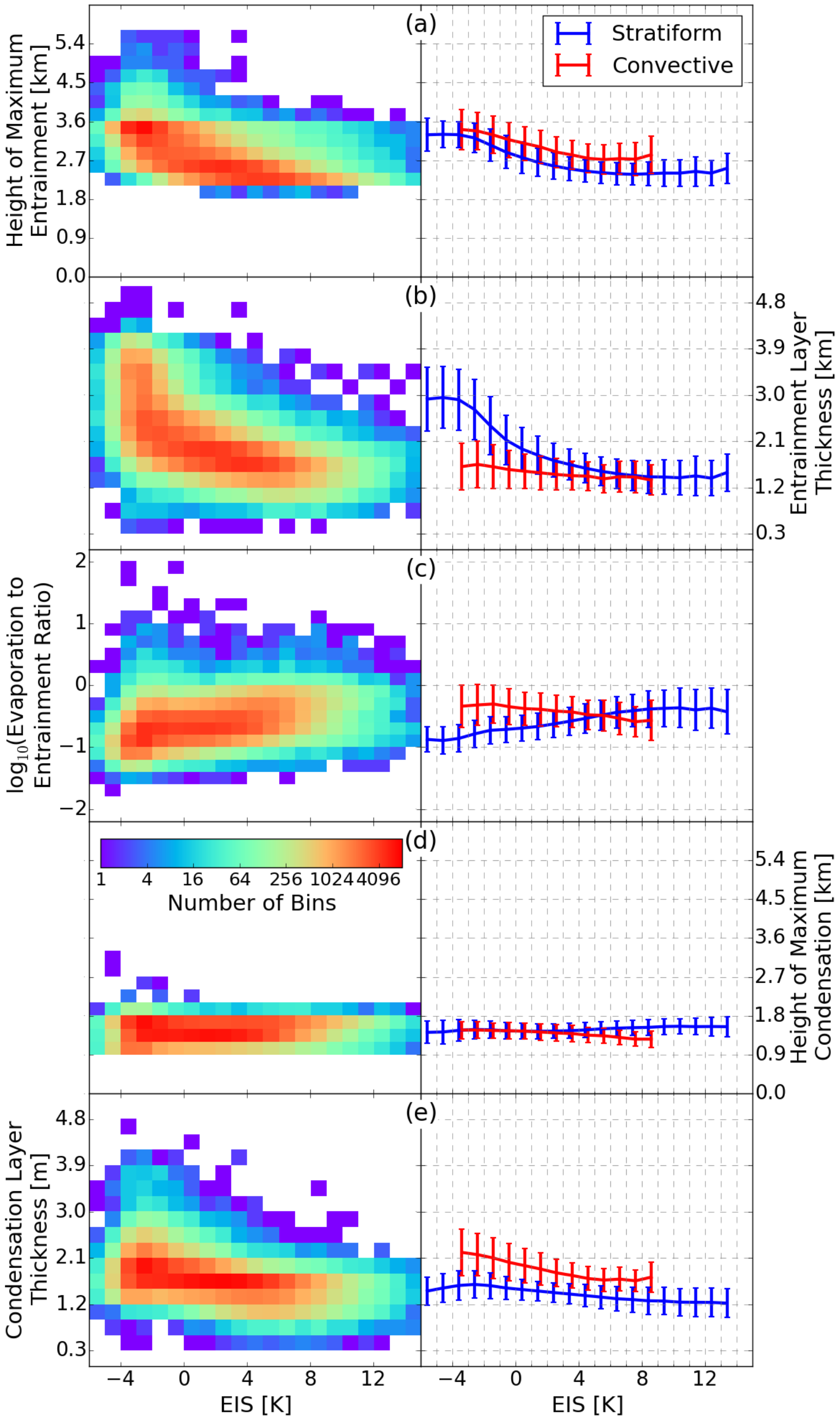

Figure 12. Joint monthly averaged grid box distributions between EIS and characteristics of the average latent heating profile for all regimes (left) as well as 1 K EIS bin mean and standard deviation separated into each regime (right). Characteristics shown are (a) height of the maximum cooling in the entraining layer above the heating, (b) depth of the cooling layer above the heating, (c) ratio of the cooling below the heating layer to the cooling above the heating layer, (d) height of the maximum condensational heating, and (e) thickness of the heating layer. Line plots are slightly offset on the abscissa for improved viewing.